

FOCAL PLANE ARRAY BEAM-FORMING AND SPILL-OVER CANCELLATION USING VIVALDI ANTENNAS

Walter Brisken (NRAO), Christophe Craeye (UCL)

January 29, 2004

Abstract Phased-array feeds are possibly the best option for the 240 to 1200 MHz band on VLA antennas due to their wide bandwidth and relatively small size. One of the greatest assets of these antennas is the ability to produce a shaped beam by appropriately phasing the elements allowing in some cases nearly uniform aperture illumination with minimal ground-directed spillover. The beam-forming properties of Vivaldi focal plane arrays are explored here using detailed calculations that account for the true beam shapes of Vivaldi elements and the geometry of the VLA antennas. We find that the beam-forming properties of Vivaldi arrays are well suited for the VLA. Some additional properties of focal plane array beam-forming are presented as well.

1 Introduction

This memo describes how Grasp8 [1] and realistic focal plane array element patterns can be used to understand better the properties of focal plane arrays. It is a follow-up to EVLA Memo 53 [2], but with much more realistic calculations. Focal plane arrays are currently being explored by a number of radio astronomy observatories. The potential for inexpensive, high performance, high bandwidth feeds, especially for radio wavelengths longer than about 5 cm is compelling.

At a discussion in Charlottesville, VA in May 2003 several unexplored details emerged, each of which could complicate the deployment of focal plane arrays for very demanding radio astronomy applications. These issues include: resistive losses, matching to LNAs, truncation effects of finite arrays, element spacing effects, manufacturing issues, noise coupling between elements, spillover cancellation, and wide-band beam-forming. The simulations presented here attempt to shed light on the spillover cancellation and beam-forming aspects of a finite array, using a realistic antenna model and realistic array element patterns. All of the simulations discussed are in the context of a 240 to 800 MHz focal plane array suitable for use on a VLA antenna.

2 Simulation

The simulations described here can be broken down into three distinct processes, explained in detail in the following sections. The first phase of the simulation is the beam pattern calculation for each element via Method of Moments (MoM). Each of these elements is then used to feed a VLA antenna from the primary focal plane. Grasp8 is then used to compute the corresponding antenna pattern for each element. Finally beam-forming is performed using the properties of the antenna beam patterns.

2.1 Conventions

Right-handed Cartesian coordinate systems are used throughout the calculations. The positive z axis is always aligned with the principle radiation axis. In several instances polar coordinate systems are used. The two coordinates are θ , the angle from the z axis, and ϕ , the azimuthal angle which is zero along the x axis and increases counter-clockwise toward the y axis. MKSA units are used (i.e., meters (m), volts (V), seconds (s), and ohms (Ω)). These calculations are performed in the transmission case. Reciprocity guarantees that the results obtained this way are correct for the receive case as well.

2.2 Element pattern calculation

The focal plane array chosen for this simulation consists of 180 Vivaldi elements arranged on a square grid. They are electrically connected with each other (cf. [3] and references therein). The eight-fold symmetry

reduces to 25 unique element radiation patterns that are computed using a MoM algorithm. The element gridding is shown in Figure 1; it is made of “Rao-Wilton-Glisson” basis functions [4]. The designations of these 25 unique elements are given in Figure 2. The remaining 155 elements’ patterns are derived from symmetry. The i th element’s radiation pattern for a one volt excitation and a 100Ω series impedance, $\vec{E}_{e,i}(\theta, \phi)$, is computed over the forward hemisphere of the elements and sampled every 4.73 degrees in θ and 18 degrees in ϕ using MoM. The 25 patterns are shown for three frequencies in Figures 22–24 in Appendix B. The array simulated consists of dielectric-free metallic plates attached to a ground plane of infinite extent. A more realistic array consisting of metal-plated dielectric on an appropriately sized ground plane will be analyzed later. The median-line symmetries of the array were exploited to reduce the complexity of the calculations, running 16 times faster and in one quarter the memory that the same calculation would have had the symmetries not been used. Somewhat more time and memory were saved by exploiting the diagonal-line symmetry as well. A special treatment was applied to the basis functions and sources crossing the planes of symmetry. Convergence towards the infinite-array solution has been verified.

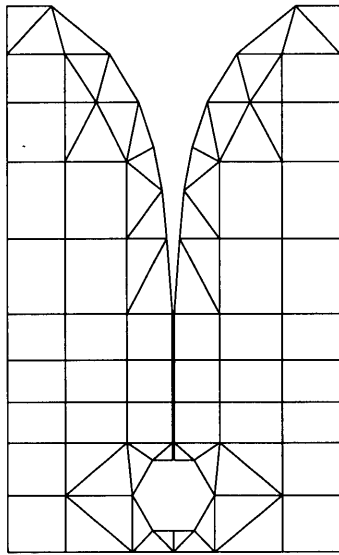


Figure 1: The MoM grid used to compute currents on each array element. 132 unknown currents computed per element in the MoM calculations.

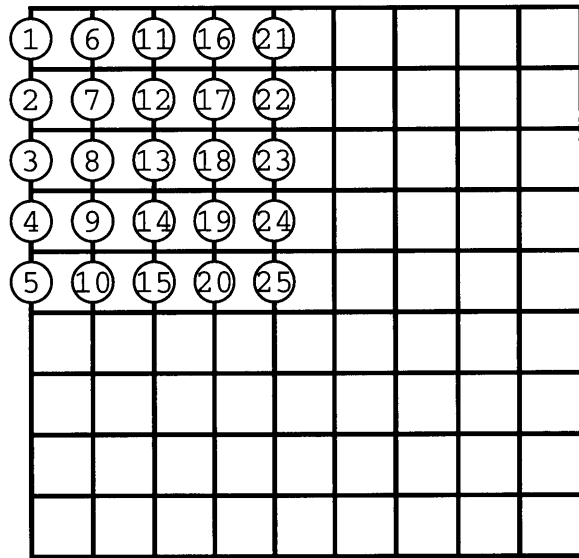


Figure 2: The locations and designations of the 25 unique elements. Each horizontal and vertical segment corresponds to one of the 180 elements in the array.

2.3 Antenna pattern calculation

The Grasp8 software package is used to compute currents on metal surfaces that are induced by radiation sources and later compute the radiation patterns of the surfaces. An exact model of a VLA antenna would be very hard to analyze due to compute time limitations and uncertainties in the scattering properties of some antenna components, so some approximations are made. Although the exact beam patterns, especially in the far sidelobes and backlobes, probably differ from those computed here, the results are still useful in understanding beam-forming and spill-over cancellation. The upgraded VLA antennas have a feed cone that stands about 1.8 m above the antenna surface with a 5° sloped roof to redirect reflected radiation away from the subreflector. It also has a 110° sector missing to allow space for the large L-band feed. In the Grasp8 model, the feed cone is represented by a circularly symmetric cone with a 5° slope that meets the dish surface at the inner edge of the panels (2 m from the center). The second approximation is at the apex of the antenna. Since the focal plane array’s scattering properties are not modeled, a model of the VLA subreflector is used as the scatterer at the apex. The combined effects of these two approximations

cannot dominate the primary beam or near sidelobe calculations. The effects of these approximations should only become important around the fifth sidelobe due to the sizes of these scatters relative to the size of the primary. It should be noted that the scattering off the support legs (struts) uses physical optics code meant for struts at least $\lambda/6$ in cross section. This condition is barely met for the lowest frequencies studied.

For each of the 25 unique element patterns, $\vec{E}_{e,i}(\theta, \phi)$, a corresponding VLA antenna pattern, $\vec{E}_{a,i}(\theta, \phi)$ is computed using the Grasp8 software package. Grasp8 computes the antenna radiation pattern by successive illuminations of sources by other sources. This requires the user to explicitly program the sequence of operations. For this application, this sequence can be summarized as:

$$\begin{array}{rcl} \text{F} & \longrightarrow & \text{L}_1 \\ \text{F, L}_1 & \longrightarrow & \text{P} \\ \text{P} & \longrightarrow & \text{L}_2 \\ \text{P, L}_2 & \longrightarrow & \text{S} \\ \text{F, P, L}_2, \text{S} & \longrightarrow & \text{B} \end{array}$$

Each arrow refers to the illumination of the scatterer on the right from the source(s) on the left side. The objects represented by letters are: feed (F), support legs (L_1 and L_2), primary reflector (P), subreflector (S), and the antenna beam (or radiation pattern) (B). The legs have two opportunities to scatter the radiation, hence the two separate simulation passes over the struts. The scripts used to drive Grasp8 are shown in Appendix A. Future studies of this kind should include the $L_1 \longrightarrow B$ scattering which was inadvertently not included in these simulations. Had this scattering been included, the computed system temperatures would probably be a bit, but not substantially, higher, due to additional scattered power.

It should be noted that at the higher frequencies, the primary is not formally in the far-field of the array since $2D_{\text{array}}^2/\lambda \simeq 11$ m, which is greater than their separation of about 9 m. At these higher frequencies the radiating portion of the array shrinks to an area on the order of one square wavelength when a single element is excited, so the use of far-field element patterns is valid.

The radiated field is calculated on two grids. The first, a full Nyquist sampled 4π steradian far-field spherical grid, is used in the beam optimization calculation as described in the next section. The second is a small oversampled far-field sine-projected beam pattern centered on $\theta = 0$ out to a couple sidelobes, used to reconstruct the beam pattern on the sky. All 25 unique antenna patterns at three specific frequencies are displayed in Figures 25–27 in Appendix C.

2.4 Beam optimization

To achieve maximum on-axis sensitivity with a radio telescope, the ratio of forward gain to system temperature (essentially a signal-to-noise ratio) is maximized. The parameters that are varied to achieve maximal gain are the complex weights assigned to each element in the array. The optimal weight vector, \vec{w} , which consists of the dimensionless element weights, w_i , is unique up to a complex scale factor. Since each linear polarization is to be independently optimized, each will have its own set of weights. The symmetries inherent in this particular problem cause the optimization of the X and Y polarizations to be equivalent, so only the case of X polarization is considered further. In practice it will likely be the two senses of circular polarization that are produced by this phasing, but the analysis follows in the same manner.

The total VLA antenna far-field radiation pattern, $\vec{E}_a(\theta, \phi)$, is a linear combination of the VLA antenna patterns corresponding to each element:

$$\vec{E}_a(\theta, \phi) = \sum_i w_i \vec{E}_{a,i}(\theta, \phi); \quad (1)$$

it is a complex-valued function with dimensions of volts. The true electric field corresponding to this antenna pattern is then

$$\vec{E}(r, \theta, \phi) = \vec{E}_a(\theta, \phi) \frac{e^{-ikr}}{r}. \quad (2)$$

From the antenna pattern, the system temperature and forward gain and thus our figure of merit can be computed. From this optimal weight vector, the pattern of the phased-array, $\vec{E}_c(\theta, \phi)$ is similarly computed:

$$\vec{E}_c(\theta, \phi) = \sum_i w_i \vec{E}_{c,i}(\theta, \phi). \quad (3)$$

From this pattern, the illumination of the primary can be examined. Also, the direct spillover onto the ground from the phased-array can be seen.

The power pattern is related to the radiation pattern by

$$\frac{dP}{d\Omega}(\theta, \phi) = \frac{1}{2\eta} \left| \vec{E}_a(\theta, \phi) \right|^2. \quad (4)$$

The free-space impedance, η is defined as $\sqrt{\mu_0/\epsilon_0}$. The total power transmitted is thus

$$P_{\text{tot}} = \int d\Omega \frac{dP}{d\Omega}(\theta, \phi). \quad (5)$$

This can be expressed as a quadratic form of the weight vector

$$P_{\text{tot}}(\vec{w}) = \vec{w}^H \cdot \mathbf{P} \cdot \vec{w}, \quad (6)$$

where the superscript H refers to the conjugate transpose and the Hermitian matrix \mathbf{P} is defined by its elements,

$$P_{ij} = \frac{1}{2\eta} \int d\Omega \vec{E}_{a,i}^* \cdot \vec{E}_{a,j}. \quad (7)$$

It is useful to note that \mathbf{P} is a positive definite matrix, meaning that all of its eigenvalues are real and positive. Likewise the X polarized power pattern is

$$\frac{dX}{d\Omega} = \frac{1}{2\eta} \left| \vec{E}_a(0, 0) \cdot \mathbf{e}_X \right|^2 \quad (8)$$

The linear X polarized forward gain, G_X , which is the numerator of the ratio to maximize, is simply

$$G_X \equiv 4\pi \frac{\frac{dX}{d\Omega}(0, 0)}{P_{\text{tot}}} = \frac{2\pi \left| \vec{E}_a(0, 0) \cdot \mathbf{e}_X \right|^2}{P_{\text{tot}}}, \quad (9)$$

where \mathbf{e}_X is the linear X polarization basis vector. Note that any polarization may be optimized by replacing \mathbf{e}_X with the appropriate basis vector. G_X may be expressed as a ratio of quadratic forms:

$$G_X(\vec{w}) = \frac{\vec{w}^H \cdot \mathbf{G}_X \cdot \vec{w}}{\vec{w}^H \cdot \mathbf{P} \cdot \vec{w}} \quad (10)$$

where the Hermitian matrix \mathbf{G}_X has elements

$$G_{Xij} = \frac{2\pi}{\eta} \left(\vec{E}_{a,i}(0, 0) \cdot \mathbf{e}_X \right)^* \left(\vec{E}_{a,j}(0, 0) \cdot \mathbf{e}_X \right) \quad (11)$$

Because $G_X(\vec{w})$ must be real and can never be less than zero, all eigenvalues of \mathbf{G}_X must be real and non-negative.

The system temperature is the numerator of the ratio to optimize and consists of a constant receiver temperature, T_{rec} added to the radiation temperature seen by the receiver. For all simulations, a value for T_{rec} of 20 K was used. If an array of this type is to be competitive with a high-performance horn antenna, a value not much greater than this must be realized in the hardware. It is implicitly assumed that the receiver noise in each element is uncorrelated with that of other elements. The radiation temperature is the gain-weighted average of the surrounding radiation temperature. The radiation temperature model that will be used here is

$$T_{\text{rad}}(\theta, \phi) = \begin{cases} T_{\text{sky}} & \text{above ground} \\ T_{\text{ground}} & \text{below ground} \end{cases}, \quad (12)$$

where $T_{\text{ground}} = 290\text{K}$ and $T_{\text{sky}} = \nu[\text{GHz}]^{-2.5} \times 3\text{K}$ for frequencies below 1 GHz, and $T_{\text{sky}} = 3\text{K}$ above 1 GHz. All simulations were done the the antenna pointing at the zenith. With this temperature model, the system temperature can be computed as

$$T = \frac{\int d\Omega (T_{\text{rad}}(\theta, \phi) + T_{\text{rec}}) P(\theta, \phi)}{P_{\text{tot}}}. \quad (13)$$

This can also be expressed as a ratio of quadratic forms:

$$T(\vec{w}) = \frac{\vec{w}^H \cdot \mathbf{T} \cdot \vec{w}}{\vec{w}^H \cdot \mathbf{P} \cdot \vec{w}} \quad (14)$$

where the positive-definite Hermitian matrix \mathbf{T} consists of elements

$$T_{ij} = \frac{1}{2\eta} \int d\Omega (T_{\text{rad}}(\theta, \phi) + T_{\text{rec}}) \vec{E}_{a,i}^*(\theta, \phi) \cdot \vec{E}_{a,j}(\theta, \phi). \quad (15)$$

For an infinitesimal bandwidth, the quantity to be maximized in order to produce the most sensitive beam is the ratio, $R(\vec{w})$, of linear X polarized forward gain to the system temperature, or

$$R(\vec{w}) \equiv \frac{G_X(\vec{w})}{T(\vec{w})} = \frac{\vec{w}^H \cdot \mathbf{G}_X \cdot \vec{w}}{\vec{w}^H \cdot \mathbf{T} \cdot \vec{w}}. \quad (16)$$

Since the matrix \mathbf{T} is positive definite and Hermitian, it can be expressed as the product of a lower triangular matrix, \mathbf{L} and its conjugate transpose, \mathbf{L}^H , (i.e., $\mathbf{T} = \mathbf{L} \cdot \mathbf{L}^H$) by Cholesky decomposition. Thus, with a change of basis,

$$\vec{w} = \mathbf{L}^{H^{-1}} \cdot \vec{z} \quad (17)$$

$$\vec{w}^H = \vec{z}^H \cdot \mathbf{L}^{-1} \quad (18)$$

$$\mathbf{G}_X = \mathbf{L} \cdot \mathbf{M} \cdot \mathbf{L}^H \quad (19)$$

R can be rewritten as

$$R(\vec{z}) = \frac{\vec{z}^H \cdot \mathbf{M} \cdot \vec{z}}{\vec{z}^H \cdot \vec{z}}. \quad (20)$$

It is clear that $R(\vec{z})$ is greatest when z is proportional to the eigenvector of \mathbf{M} corresponding to the greatest eigenvalue. In fact, the greatest value that $R(\vec{z})$ can attain is the greatest eigenvalue of \mathbf{M} . Because (a) both \mathbf{G}_X and \mathbf{T} are Hermitian, (b) \mathbf{T} is positive definite, and (c) \mathbf{G}_X is non-negative definite, all eigenvalues of \mathbf{M} must be real and non-negative. The greatest eigenvector can be isolated by repeatedly multiplying a guess value of z by the matrix \mathbf{M} . For the application here, the greatest eigenvalue is greater than the second-greatest eigenvalue by many orders of magnitude, so after only a couple such multiplications, the vector result will converge to the greatest eigenvector. To ensure that the guess vector contains some contribution from the greatest eigenvector, many randomly generated vectors are screened; the best performing of these vectors is then used as the guess vector. This method is often called the *Power Method* [5]. The optimal value of \vec{w} is then determined though Eqn. 17 after the repeated multiplication (i.e., $\vec{w}_{\text{opt}} = \mathbf{L}^{H^{-1}} \cdot \mathbf{M}^n \cdot \vec{z}_{\text{guess}}$ for large n). A very similar method has been applied to adaptive beam-forming for mobile communications [6].

3 Results of optimizations

Optimization was performed at eight frequencies: 266, 288, 311, 460, 480, 500, 760, and 780 MHz. Several performance parameters for these frequencies are tabulated in Table 1. Note that the performance at 780 MHz is far worse than at 760 MHz. It appears that something went awry in the generation of antenna patterns from the element patterns (something didn't converge?) The 780 MHz data will not be further considered here.

More detailed plots for 311, 500, and 760 MHz follow in Figures 4–15. For each of these frequencies, the optimized phased-array pattern, \vec{E}_e , and the corresponding antenna pattern, \vec{E}_a are shown. Also shown are the azimuthally averaged antenna pattern spanning the full 180° of boresight angles and a diagram showing the optimized weight vectors. The spillover cancellation is shown dramatically in Figures 6, 10, and 14.

ν	(MHz)	266	288	311	460	480	500	760	780
λ	(m)	1.124	1.038	0.964	0.652	0.625	0.600	0.394	0.384
T_{rec}	(K)	20	20	20	20	20	20	20	20
T_{sky}	(K)	82.2	67.4	55.6	20.9	18.8	17.0	6.0	5.6
T_{ground}	(K)	290	290	290	290	290	290	290	290
Gain	(dBi)	36.3	37.0	37.6	40.8	41.1	41.5	44.7	42.8
A_{eff}	(m ²)	425.3	426.8	422.6	407.0	403.9	403.5	362.2	223.3
η		0.87	0.87	0.86	0.83	0.82	0.82	0.74	0.45
T_{sys}	(K)	107.6	91.9	80.0	43.9	41.6	39.8	29.1	56.9
T_{spill}	(K)	5.3	4.5	4.4	3.0	2.8	2.8	3.1	31.3
$A_{\text{eff}}/T_{\text{sys}}$	(m ² /K)	3.95	4.65	5.28	9.26	9.72	10.14	12.46	3.93

Table 1: Parameters of the array at the eight frequencies studied. The top section contains the parameters used in for that column’s optimization. The bottom section contains the resultant performance parameters after optimization. Efficiency, η , is the effective area, A_{eff} , divided by the unblocked aperture area (490.1 m² for a VLA antenna). The figure of merit that is optimized is effective area divided by system temperature. The spillover temperature, T_{spill} , is defined here as $T_{\text{sys}} - T_{\text{rec}} - T_{\text{sky}}$.

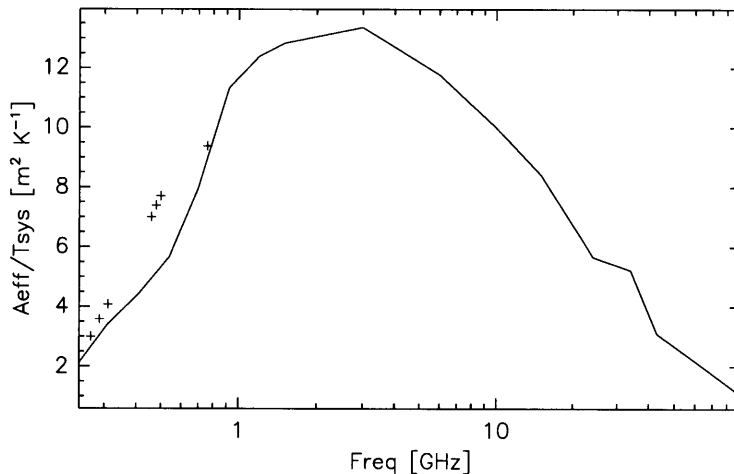


Figure 3: The EVLA sensitivity goal (solid line) and the estimated focal plane array performance (marks) at 266, 288, 311, 460, 480, 500, and 760 MHz. 80% of the calculated performance is used as the estimate for these frequencies, allowing for some resistive loss, phasing inefficiency, and other processing losses.

4 Tuning range

The useful tuning range of the array is limited by its performance at the extremes. At the lower frequencies explored, the wavelength approaches the array’s size. This reduces the array’s ability to efficiently illuminate the primary. This is because exciting the higher phased-array pattern multipoles become less easily excited. At higher frequencies where the wavelength is less than about two element spacings, grating lobes are formed causing higher system temperature due to insufficient sampling of the focal plane field. The power that is redirected to sidelobes is taken from the intended primary beam. For the array studied, the useful tuning range spans the frequencies studied, but does not likely extend much below 240 MHz ($\lambda = 1.2$ m) or above 800 MHz ($\lambda = 0.38$ m). A physically larger array would be required to extend high performance to frequencies lower than ~ 240 MHz. Smaller, more densely packed elements would be needed to extend performance above 800 MHz. It would probably make sense to use two arrays to cover the full 240 to 1200 MHz frequency range.

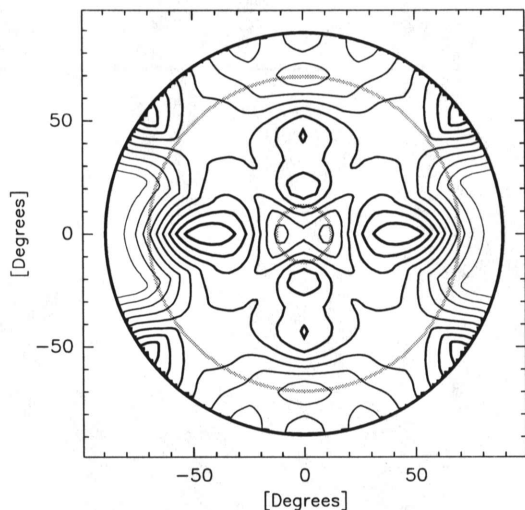


Figure 4: The phased-array pattern optimized for 311 MHz. The contours show electric field magnitude, $|\vec{E}_e|$, in the forward hemisphere of the phased array. A contour is drawn every 10% of the peak value. The inner grey circle marks angle subtended by the unpaneled portion of the primary. The outer grey circle is rim of the primary. The dark black circle denotes 90 degrees from boresight. This pattern should be compared with the individual element patterns in Figures 22 and 25.

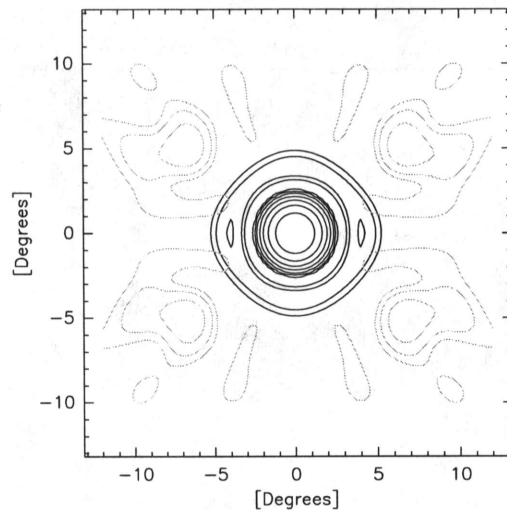


Figure 5: The antenna pattern optimized for 311 MHz. The black contours show the co-polarized gain. Contours are drawn every 3dB. The gray contours show the cross-polarized gain. Again contours are drawn every 3dB. The peak cross-polarized gain is 33dB below the peak co-polarized gain.

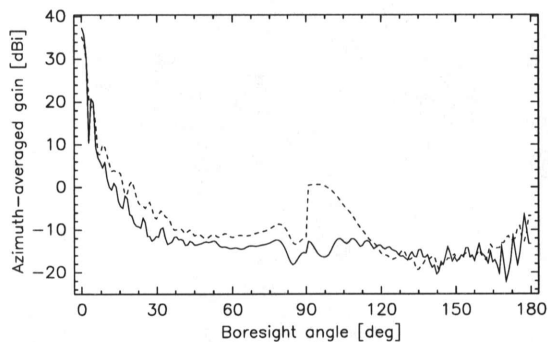


Figure 6: Azimuthally averaged power pattern at 311 MHz of a single center element (dashed) and of the optimally phased-array (solid).

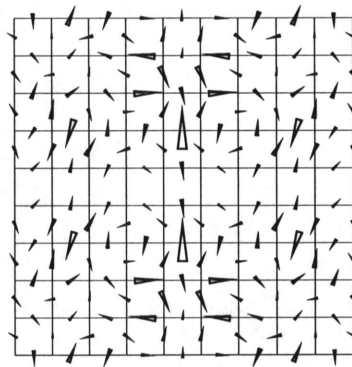


Figure 7: A representation of the optimal element weights at 311 MHz. The weight amplitude for a given element is proportional to the length of the triangle centered on that element. The phase is equal to the angle of the triangle.

5 Co-phased bandwidth

While the tuning range spans the entire range of frequencies tested, a weight vector that optimizes performance at one frequency will perform well only over a relatively small band about that frequency. Table 2

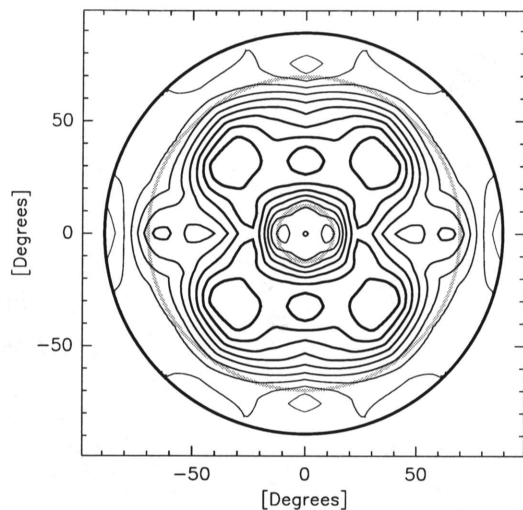


Figure 8: The phased-array pattern optimized for 500 MHz. Note that optimization reduces the power hitting the feed cone as this portion of the primary does not contribute to forward gain.

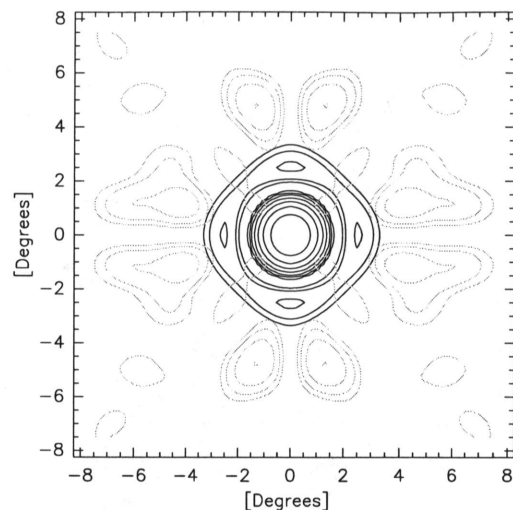


Figure 9: The 500 MHz optimized antenna pattern. The peak cross-polarized gain (gray contours) is 32dB lower than the peak co-polarized gain (black contours). Contours are spaced at 3dB intervals.

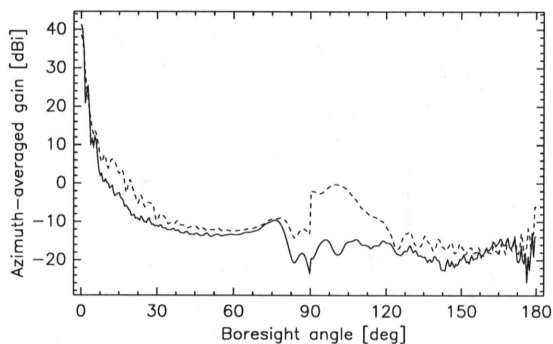


Figure 10: Azimuthally averaged power pattern at 500 MHz of a single center element (dashed) and of the optimally phased-array (solid).

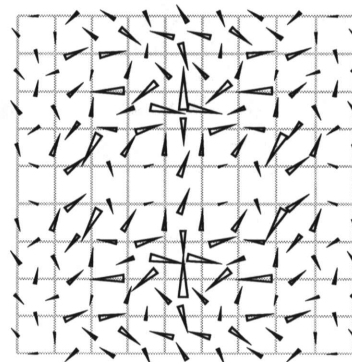


Figure 11: The weight pattern at 500 MHz.

shows η_{phase} the ratio of the performance at the test frequency, ν_{test} , using the weight vector from the optimize frequency, ν_{opt} , to the performance using weights optimized for ν_{test} .

Table 2 suggests that around 500 MHz, the 70% performance bandwidth is about 65 MHz, or 13%. The 50% performance bandwidth is estimated to be about 100 MHz, or 20%. Simply tapering the weights of the outer array elements may increase the phasing efficiency at a minimal cost of center frequency performance since these weights change most rapidly with frequency.

A generally better and more uniform performance across a band of interest could likely be obtained by optimizing over a finite bandwidth ($\delta\nu$ of bandwidth at center frequency ν_0). In the continuum limit, such

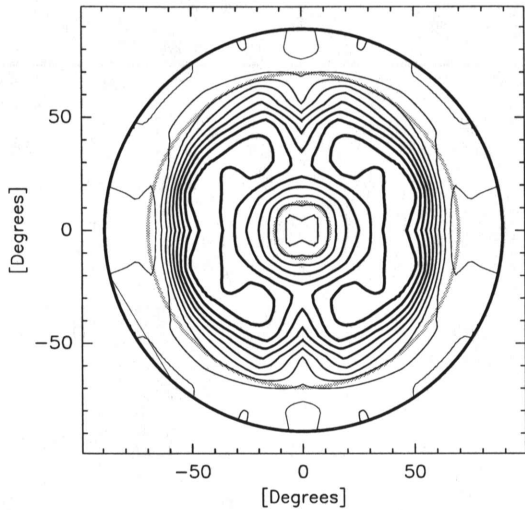


Figure 12: The phased-array pattern optimized for 760 MHz.

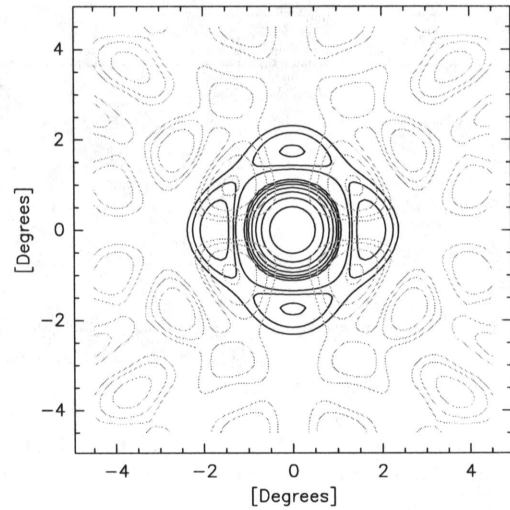


Figure 13: The 760 MHz optimized antenna pattern. The peak cross-polarized gain (gray contours) is 32dB lower than the peak co-polarized gain (black contours). Contours are spaced at 3dB intervals.

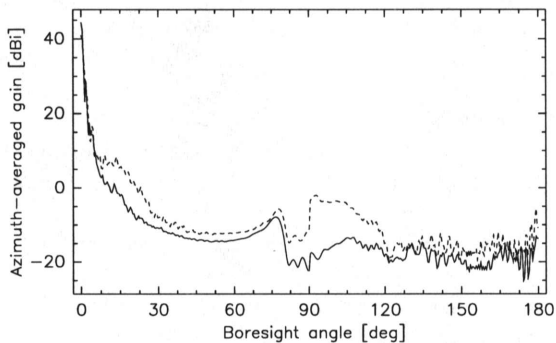


Figure 14: Azimuthally averaged power pattern at 760 MHz of a single center element (dashed) and of the optimally phased-array (solid). The increase in gain around 75° is due to scattering off the struts. Enhanced gain between about 9 and 30° arises from diffraction around the secondary. Note that the phased beam illuminates the subreflector much less than the just the central element and thus has much reduced scattered power in this angular range.

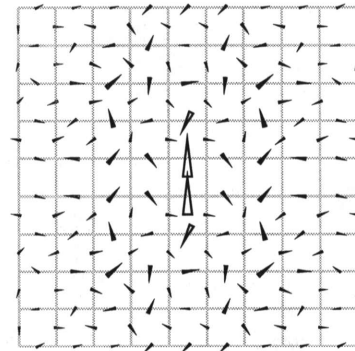


Figure 15: The weight pattern at 760 MHz.

a function to optimize might be

$$R(\vec{w}; \nu_0, \delta\nu) = \int_{\nu_0 - \delta\nu/2}^{\nu_0 + \delta\nu/2} d\nu W(\nu) \frac{\vec{w}^H \cdot \mathbf{G}_X(\nu) \cdot \vec{w}}{\vec{w}^H \cdot \mathbf{T}(\nu) \cdot \vec{w}}, \quad (21)$$

ν_{opt}	(MHz)	266	266	288	288	460	460	480	480	500
ν_{test}	(MHz)	288	311	266	311	480	500	460	500	460
Gain	(dBi)	36.2	34.0	35.7	35.9	40.7	40.1	40.8	41.1	40.6
A_{eff}	(m ²)	362.6	187.5	376.2	285.4	368.7	289.7	405.2	369.6	389.1
T_{sys}	(K)	102.8	127.9	124.6	106.6	46.1	63.0	49.9	45.72	62.2
T_{spill}	(K)	15.4	52.2	22.4	31.0	7.3	26.0	9.0	8.75	21.3
$A_{\text{eff}}/T_{\text{sys}}$	(m ² /K)	3.53	1.47	3.02	2.68	7.99	4.60	8.12	6.26	8.08
η_{phase}		0.76	0.28	0.76	0.51	0.82	0.45	0.88	0.80	0.68

Table 2: Table showing performance measured at frequency ν_{test} for an array optimized for best performance at frequency ν_{opt} . The fractional performance loss due to this mismatch is the “phasing efficiency”, η_{phase} .

where $W(\nu)$ is a band shaping function that can be used to match the bandpass to a desired form and the two Hermitian matrices have gained frequency dependence. Optimizing this is no longer a simple exercise. True wide-band optimization will be deferred to a future test.

6 Phased-Array Field of view

The performance optimization can be performed for Gains in directions other than boresight. By replacing the boresight direction (0, 0) in Eqn. 11 with a general direction, $(\theta_{\text{beam}}, \phi_{\text{beam}})$, performance can be optimized for any desired direction. One may wish to observe off axis if there are multiple targets within the phased-array field of view that span multiple primary beams and if the back-end electronics can handle multiple simultaneous array phasings. The best attainable performance for an offset beam depends on $(\theta_{\text{beam}}, \phi_{\text{beam}})$. As θ_{beam} increases, the focal spot moves away from the center of the focal plane. When a substantial fraction of the focal spot power is no longer intercepted by the array efficiency drops quickly. Also, as θ_{beam} increases, the projected area of the primary decreases, which is usually a much less substantial effect. The optimized performance as a function of beam direction at 500 MHz is shown in Figure 16. It is worth noting that the response as a function of displacement rolls off smoothly at 500 MHz. At 760 MHz, there are local maxima in the performance at displacements which center the focal spot on a receiving element, an indication that at this frequency the spacing of the elements is important (Figure 17). This can be understood as the beams in the sky narrowing as frequency increases to the point where neighboring element beams do not overlap sufficiently and the sensitivity “between the beams” worsens. Polarization performance must suffer in these circumstances since the X and Y polarized elements are not co-located. The optimized antenna pattern becomes more asymmetric with larger sidelobes as θ_{beam} increases as is shown in Figure 18. The usable field of view for the simulated array is about 4°.

7 Phasing errors

The performance of the array depends on the precision of the phasing. Errors in characterizing the absolute patterns, including phase, and in setting weights will lead to weighting errors. The effect of weighting errors is explored here by randomly dithering optimal weights. Independent normal-distributed errors were added to the real and imaginary parts of each weight ranging in magnitude from zero to 10% of the value of the greatest weight and the sensitivity was evaluated. This was repeated 1000 times for each error magnitude. The mean sensitivity (solid line) and the sensitivity range encountered (gray region) are shown in Figures 19–21.

Depending on the mechanism used to phase the array, different forms of phase errors may be more important. Table 3 summarizes the effects of pure phase errors and pure amplitude errors. Here the amplitude errors are relative to each weight’s amplitude, rather than the amplitude of the greatest weight. The errors are again drawn from Normal distributions. The amplitudes of these errors causing 1dB and 3dB performance losses are listed.

The 311 MHz data is most sensitive to phasing errors. This likely arises from the extreme oversampling (i.e., more degrees of freedom exist than are required to fully sample the focal plane) that occurs at this low

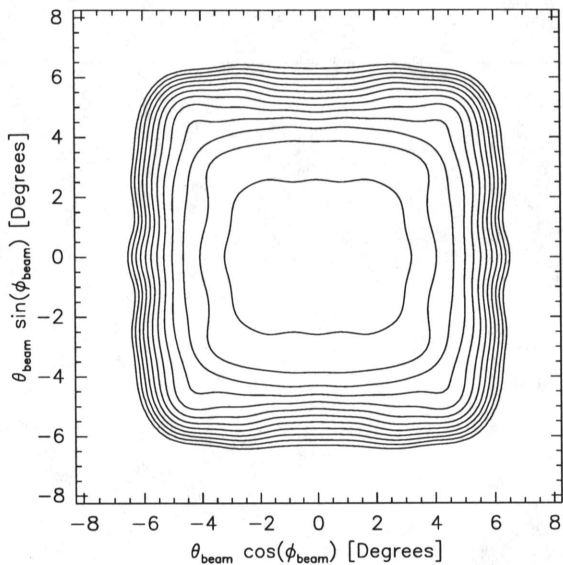


Figure 16: 500 MHz optimal performance as a function of beam placement. The innermost contour represents 1.5dB performance loss, about 3° from bore-sight. Each additional contour is 1.5dB worse. At about 4° the center of the focal spot leaves the focal plane.

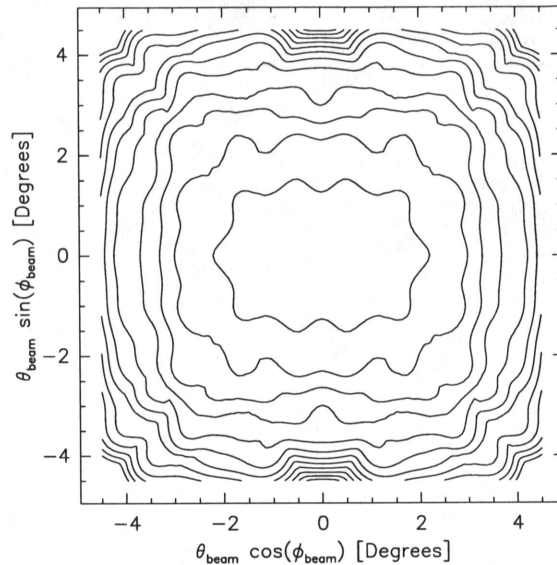


Figure 17: 760 MHz optimal performance as a function of beam placement. The innermost contour represents 1dB performance loss, about 3° from bore-sight. Each additional contour is 1dB worse. At this frequency the element spacing is approaching $\lambda/2$ and spacing effects cause the corrugated performance which peaks when the focal spot centers on an element.

	ν	(MHz)	311	500	760
Phase errors	1dB loss	(deg)	6	6.5	18
	3dB loss	(deg)	11	18	35
Amp. errors	1dB loss	(%)	3.5	11	33
	3dB loss	(%)	6.5	22	65

Table 3: The effect of pure phase errors and pure amplitude errors on performance. The values in the table reflect the tolerances for the two types of errors required to achieve performance within 1dB and 3dB of the expected performance. For example, on average an 18 degree RMS phase error will reduce the 500 MHz performance by 3dB.

frequency which causes neighboring elements to be nearly degenerate. The addition of $+\delta w$ to one element's weight and $-\delta w$ to its neighbor's has almost no effect on the phased antenna pattern in over-sampled cases. However, the addition of antisymmetric weights to neighboring elements makes the phasing more sensitive to phasing errors. It is seen that optimization takes advantage of these extra degrees of freedom and results in a weight pattern with significantly anti-correlated neighboring weights as is shown in Figure 7.

Thus it is seen that the optimal weights derived for the lower frequencies are optimal only in a theoretical sense. More stable weights with greater phasing bandwidths and a less stringent requirement on front end linearity and dynamic range, are likely possible to derive by enforcing more smoothly varying weights or by optimizing over a finite bandwidth. This may come at a modest cost in center frequency performance.

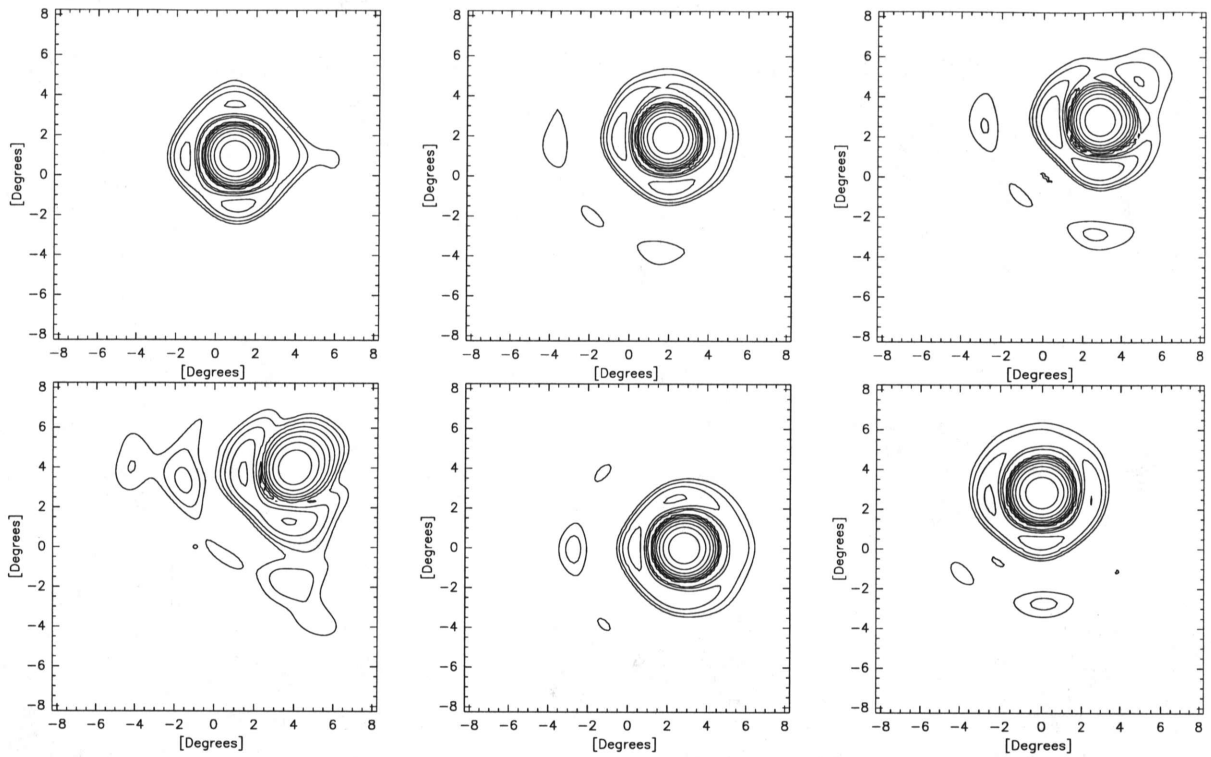


Figure 18: 500 MHz beam shapes produced when forming beams off boresight. The displacements are in the top row, left to right: $(1^\circ, 1^\circ)$, $(2^\circ, 2^\circ)$, and $(3^\circ, 3^\circ)$, and in the bottom row, left to right: $(4^\circ, 4^\circ)$, $(3^\circ, 0^\circ)$, $(0^\circ, 3^\circ)$. Note that the beam starts to degrade quickly once the displacement reaches about 4° . All contours are at 3dB intervals starting 3dB below the peak gain.

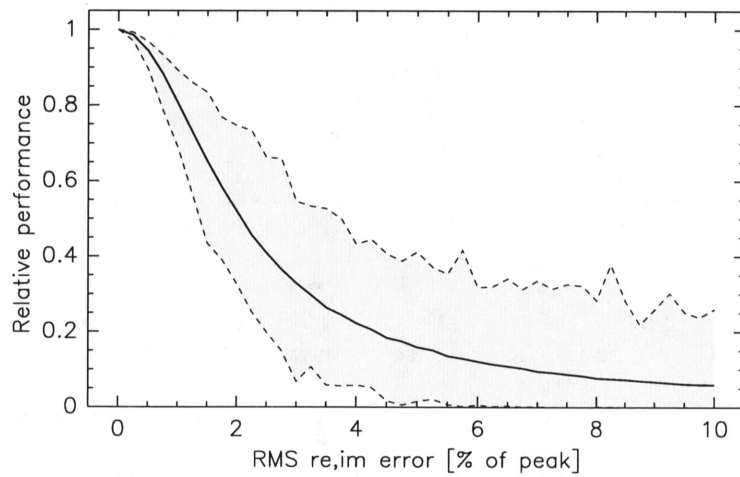


Figure 19: The effect of phasing errors on performance at 311 MHz. The solid line is the mean sensitivity relative to the optimal weight vector for weight perturbations up to 10% of the value of the greatest element weight. The shaded area represents the range of sensitivities encountered by the 1000 trials.

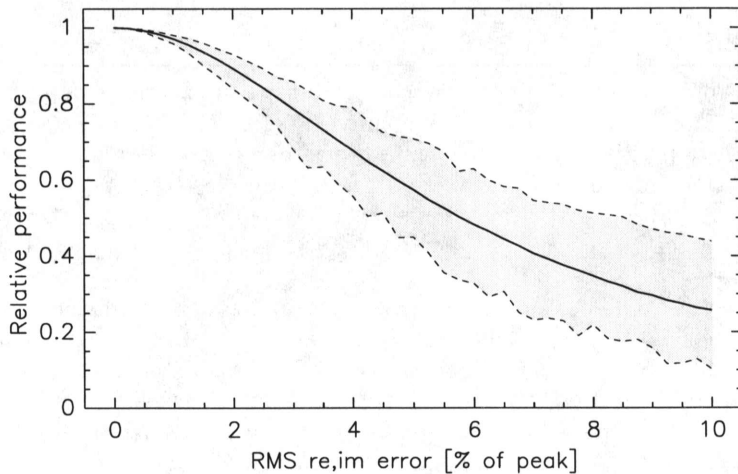


Figure 20: The effect of phasing errors on performance at 500 MHz.

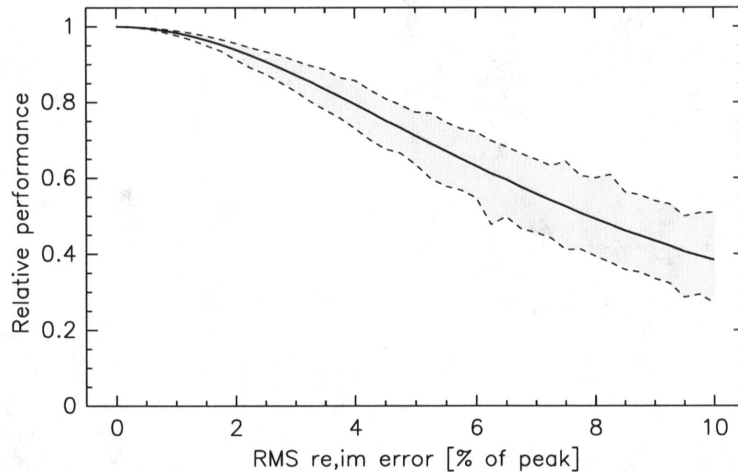


Figure 21: The effect of phasing errors on performance at 760 MHz.

8 Nulling

A current hot topic in radio frequency interference mitigation is nulling the antenna response in the direction of a known interferer, $(\theta_{\text{int}}, \phi_{\text{int}})$. This can be naturally incorporated in the formulation of optimization in Section 2.4 by adding to the radiation temperature, $T_{\text{rad}}(\theta, \phi)$ an additional contribution from this unwanted source:

$$T_{\text{int}}(\theta, \phi) = K \delta(\theta - \theta_{\text{int}}) \delta(\phi - \phi_{\text{int}}), \quad (22)$$

where K is a very large number; in particular, its value should be the equivalent brightness temperature of the RFI source. The Dirac delta functions above could be replaced with any pattern representing the true extent of the interferer if it is not a point. The null is made deeper with a larger value of K . The on-axis performance decreases as the null is made deeper and wider. Multiple interferers can be simultaneously nulled, with a correspondingly larger impact on performance.

9 Conclusions

The simulated array appears to perform well over a substantial tuning range and has a useful co-phased bandwidth of at least 13%. The performance is comparable to or better than other options for low frequency feeds for the VLA. These positive results hinge on a few assumptions. Here we assumed that the receiver temperature is 20 K at room temperature. Performance at this level has yet to be demonstrated. The combination of matching and resistive loss is assumed small enough to ignore. For this feed to be competitive with high performance (and expensive to deploy) prime focus horn receivers, these losses must not exceed about 25%.

There is still more work to do before Vivaldi arrays as focal plane feeds are understood at a useful level. Three major questions should be addressed in upcoming studies : (1) How can the array be optimized over a wider bandwidth with a given set of weights? (2) How effective is interference nulling and what impact does it have on performance. (3) How does receiver noise coupling affect performance? Practical experience using hardware will help understand additional aspects such as noise coupling, resistive losses, manufacturing issues, dynamic range/linearity requirements for the front ends, and achievable phasing precision.

10 Acknowledgments

Once again, the DRAO and its staff have been kind in hosting my visit to Penticton where much of the computation was performed. Bruce Veidt led me to pursue the interesting subject of weighting errors, a practicality that was not initially considered. The element mesh (Figure 1) was generated by Xavier Dardenne (UCL).

References

- [1] Tlcra Software, <http://www.tlcra.com>.
- [2] W. F. Brisken, "A Vivaldi Focal Plane Array for EVLA", EVLA Memo 53, May 2003.
- [3] C. Craeye & X. Dardenne, "Efficient computation of the polarization characteristics of infinite and finite arrays of tapered-slot antennas," *Proc. of IEEE Phased Array Systems and Technology Symposium*, Boston, October 2003.
- [4] S.M. Rao, D.R. Wilton, & A.W. Glisson, "Electromagnetic scattering by surfaces of arbitrary shape," *IEEE Transactions of Antennas & Propagation*, vol. 30, pp. 409-418, May 1982.
- [5] <http://www.google.com>, search for "eigenvector power method".
- [6] V. Hasu, "Eigenvalue Approach To Joint Power Control And Beamforming For CDMA Systems," *2002 IEEE Seventh International Symposium on Spread Spectrum Techniques and Applications*, vol. 2, pp. 561-565.

A Grasp8 input files

In this section, example Grasp8 files are shown. Only the script portion for element 12 evaluated at 500 MHz is shown. The following is the Grasp8 "Tlcra Object Repository" or ".tor" file used to describe the geometry of the feed, antenna, and the two grid surfaces on which fields were computed. Note that the input files `vla_pri.sfc` and `500MHz_feed_12.cut` are not listed here due to their length.

```
Field_Frequency frequency
(
  list_freq      : sequence(0.500000 GHz)
)
```

```

VLA_pri_surf rotational
(
  file_name : vla_pri.sfc,
  r_unit    : m,
  z_unit    : m,
  r_factor  : 1.0,
  z_factor  : 1.0,
  n_points  : 500,
  tip       : off,
  list      : off
)
VLA_pri_rim elliptical_rim
(
  centre     : struct(x:0 m, y:0 m),
  half_axis  : struct(x:12.5 m, y:12.5 m),
  rotation   : 0
)
VLA_primary reflector
(
  surface    : ref(VLA_pri_surf),
  rim        : ref(VLA_pri_rim)
)

VLA_pri_PO_12 standard_po
(
  frequency   : ref(Field_Frequency),
  scatterer   : ref(VLA_primary),
  po_points   : struct(po1:150, po2:400),
  ptd_points  : sequence(struct(edge:1, ptd:4
  file_name   : VLA_pri_12.cur
)

VLA_sub_surf regular_grid
(
  file_name : vla_sub.sfc,
  xy_unit   : m,
  z_unit    : m,
  xy_factor : 1.0,
  z_factor  : 1.0,
  list      : off,
)
VLA_sub_rim elliptical_rim
(
  centre     : struct(x:-0.115561 m, y:0 m),
  half_axis  : struct(x:1.163585 m, y:1.15210
  rotation   : 0
)
VLA_sub reflector
(
  surface    : ref(VLA_sub_surf),
  rim        : ref(VLA_sub_rim),
  centre_hole_radius : 0 m
)
VLA_sub_PO standard_po
(
  frequency   : ref(Field_Frequency),
  scatterer   : ref(VLA_sub),
  po_points   : struct(po1:30, po2:90),

```

```

    ptd_points : sequence(struct(edge:1, ptd:90)),
)

Strut_Coor_Sys_1 coor_sys
(
    origin : struct(x:7.550000 m, y:0.000000 m, z:1.594036 m),
    x_axis : struct(x:0.777846, y:0.000000, z:0.628455),
    y_axis : struct(x:-0.000000, y:1.000000, z:0.000000)
)

Strut_Coor_Sys_2 coor_sys
(
    origin : struct(x:0.000000 m, y:7.550000 m, z:1.594036 m),
    x_axis : struct(x:0.000000, y:0.777846, z:0.628455),
    y_axis : struct(x:-1.000000, y:0.000000, z:0.000000)
)

Strut_Coor_Sys_3 coor_sys
(
    origin : struct(x:-7.550000 m, y:0.000000 m, z:1.594036 m),
    x_axis : struct(x:-0.777846, y:0.000000, z:0.628455),
    y_axis : struct(x:-0.000000, y:-1.000000, z:0.000000)
)

Strut_Coor_Sys_4 coor_sys
(
    origin : struct(x:-0.000000 m, y:-7.550000 m, z:1.594036 m),
    x_axis : struct(x:-0.000000, y:-0.777846, z:0.628455),
    y_axis : struct(x:1.000000, y:-0.000000, z:0.000000)
)

VLA_struts polygonal_struts
(
    cross_section : sequence(
        struct(x:0.400000 m, y:0.135000 m),
        struct(x:0.000000 m, y:0.135000 m),
        struct(x:0.000000 m, y:-0.135000 m),
        struct(x:0.400000 m, y:-0.135000 m) ),
    position : sequence(
        struct(coor_sys:ref(Strut_Coor_Sys_1), z1:0 m, z2:9.799569 m),
        struct(coor_sys:ref(Strut_Coor_Sys_2), z1:0 m, z2:9.799569 m),
        struct(coor_sys:ref(Strut_Coor_Sys_3), z1:0 m, z2:9.799569 m),
        struct(coor_sys:ref(Strut_Coor_Sys_4), z1:0 m, z2:9.799569 m) )
)

VLA_struts_PO polygonal_struts_po
(
    frequency : ref(Field_Frequency),
    scatterer : ref(VLA_struts),
    po_points : sequence(struct(side:-1, n_length:80, n_phi:6) ),
    ptd_points : sequence(struct(edge:-1, ptd:80) ),
)

Feed_Coor_Sys_12 coor_sys
(
    origin : struct(x:0.000000 m, y:-0.630000 m, z:9.000000 m),
    x_axis : struct(x:1.000000, y:0.000000, z:0.000000),
    y_axis : struct(x:0.000000, y:-1.000000, z:0.000000)
)

```



```

)
Feed_Pattern_12 tabulated_feed
(
  frequency      : ref(Field_Frequency),
  file_name      : 500MHz_feed_12.cut
)
Feed_System_12 feed
(
  coor_sys       : ref(Feed_Coor_Sys_12),
  feed_definition : ref(Feed_Pattern_12),
  frequency      : ref(Field_Frequency)
)

Full_Beam_12 spherical_field_grid
(
  frequency      : ref(Field_Frequency),
  grid_type      : theta_phi,
  x_range        : struct(start:0, end:179.250000, np:240),
  y_range        : struct(start:0, end:359.462687, np:670),
  polarisation   : theta_phi,
  file_name      : 500MHz_full_beam_12.grd
)

Beam_12 spherical_field_grid
(
  frequency      : ref(Field_Frequency),
  grid_type      : uv,
  x_range        : struct(start:-0.130900, end:0.130900, np:79),
  y_range        : struct(start:-0.130900, end:0.130900, np:79),
  polarisation   : linear,
  file_name      : 500MHz_beam_12.grd
)

```

Below is the "Ticra Command Input" or ".tci" file that executes the antenna ana

```

FILES READ ALL "C:\Documents and Settings\brisken\Desktop\500MHz\500MHz.tor"
#
COMMAND OBJECT VLA_struts_PO get_currents ( source : ref(Feed_System_12)) Cmd_1
COMMAND OBJECT VLA_pri_PO_12 get_composite_currents ( source : &
  sequence(ref(Feed_System_12),ref(VLA_struts_PO))) Cmd_134
COMMAND OBJECT VLA_struts_PO get_composite_currents ( source : &
  sequence(ref(Feed_System_12),ref(VLA_pri_PO_12))) Cmd_135
COMMAND OBJECT VLA_sub_PO get_composite_currents ( source : &
  sequence(ref(VLA_struts_PO),ref(VLA_pri_PO_12))) Cmd_136
COMMAND OBJECT Full_Beam_12 get_field ( source : ref(Feed_System_12)) Cmd_137
COMMAND OBJECT Full_Beam_12 add_field ( source : ref(VLA_pri_PO_12)) Cmd_138
COMMAND OBJECT Full_Beam_12 add_field ( source : ref(VLA_sub_PO)) Cmd_139
COMMAND OBJECT Full_Beam_12 add_field ( source : ref(VLA_struts_PO)) Cmd_140
COMMAND OBJECT Beam_12 get_field ( source : ref(Feed_System_12)) Cmd_141
COMMAND OBJECT Beam_12 add_field ( source : ref(VLA_pri_PO_12)) Cmd_142
COMMAND OBJECT Beam_12 add_field ( source : ref(VLA_sub_PO)) Cmd_143
COMMAND OBJECT Beam_12 add_field ( source : ref(VLA_struts_PO)) Cmd_144
#

```

B Element patterns

Element patterns for the 25 unique elements identified in Figure 2 are shown for 311 MHz, 500 MHz, and 760 MHz in Figures 22, 23, and 24 respectively. Note their variation with frequency and position within the array. Because the array was modeled with an infinite backplane, there is no emission from beyond 90° boresight angle, thus only the forward hemisphere is shown.

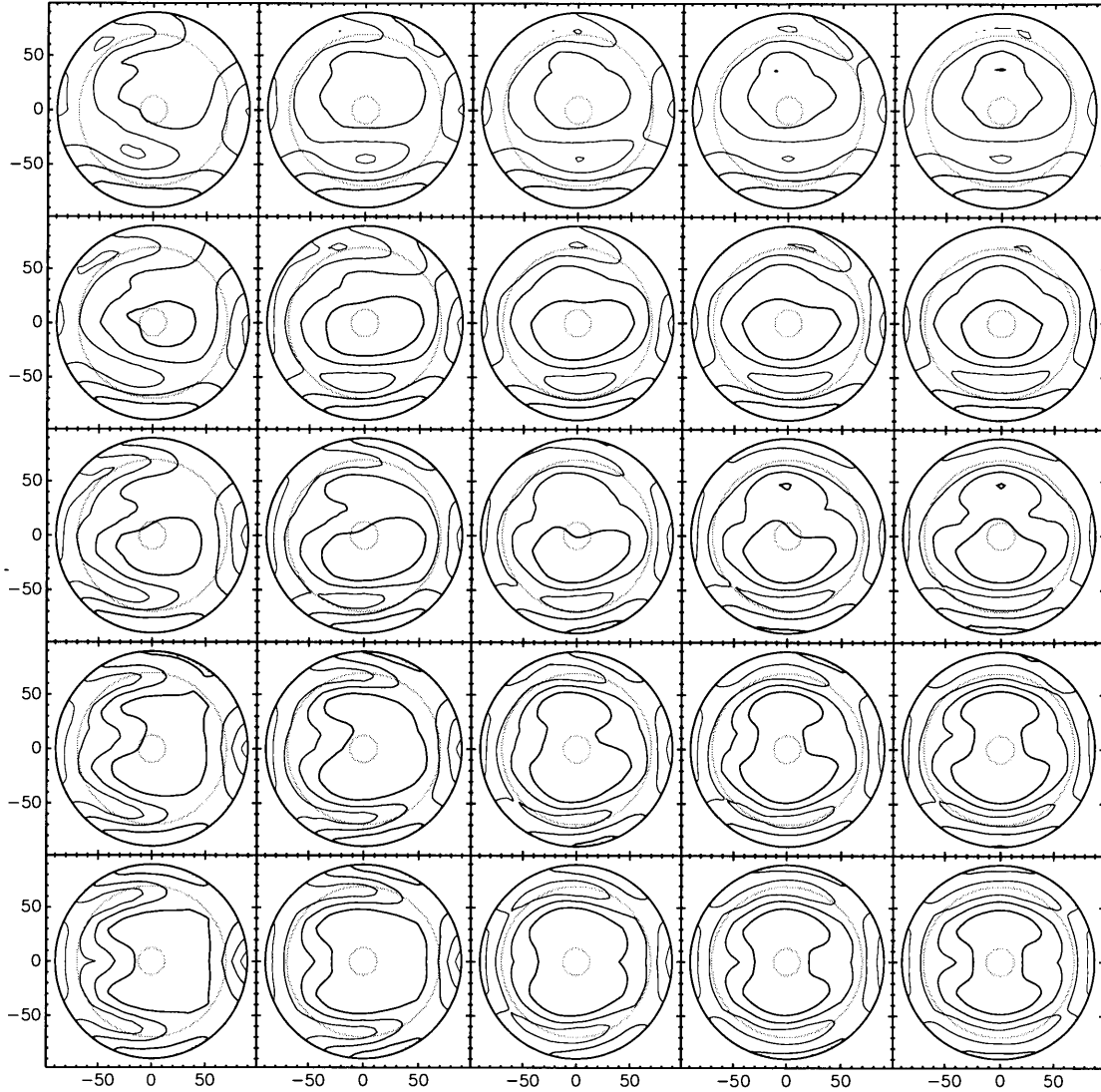


Figure 22: 25 element beam patterns at 311 MHz. Contours are drawn every 20% in voltage. The inner grey circles represent the angle subtended by the unpaneled portion of the primary. The outer grey circles represent the rim of the primary.

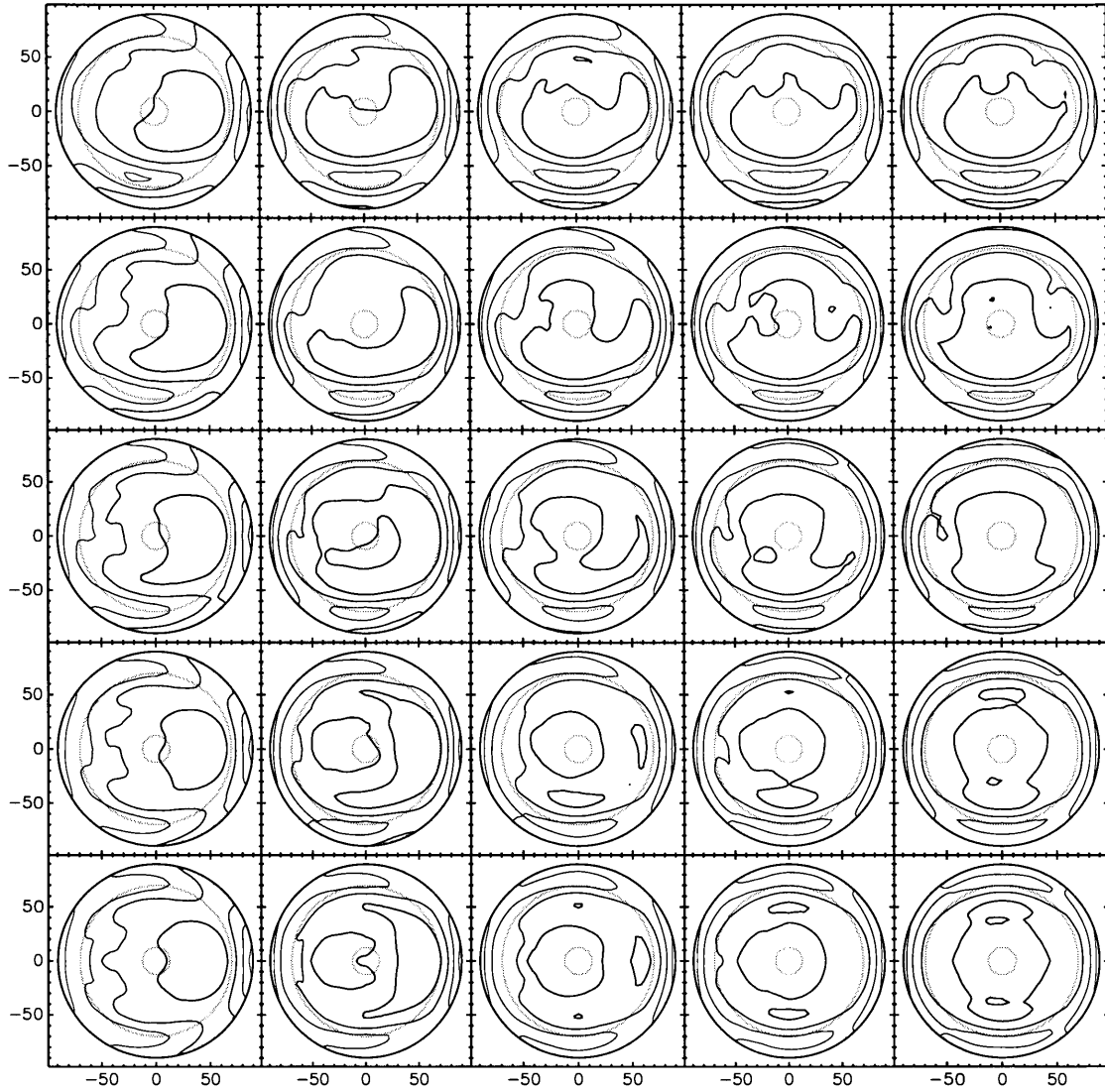


Figure 23: 25 element beam patterns at 500 MHz. Contours are drawn every 20% in voltage. The inner grey circles represent the angle subtended by the unpaneled portion of the primary. The outer grey circles represent the rim of the primary.

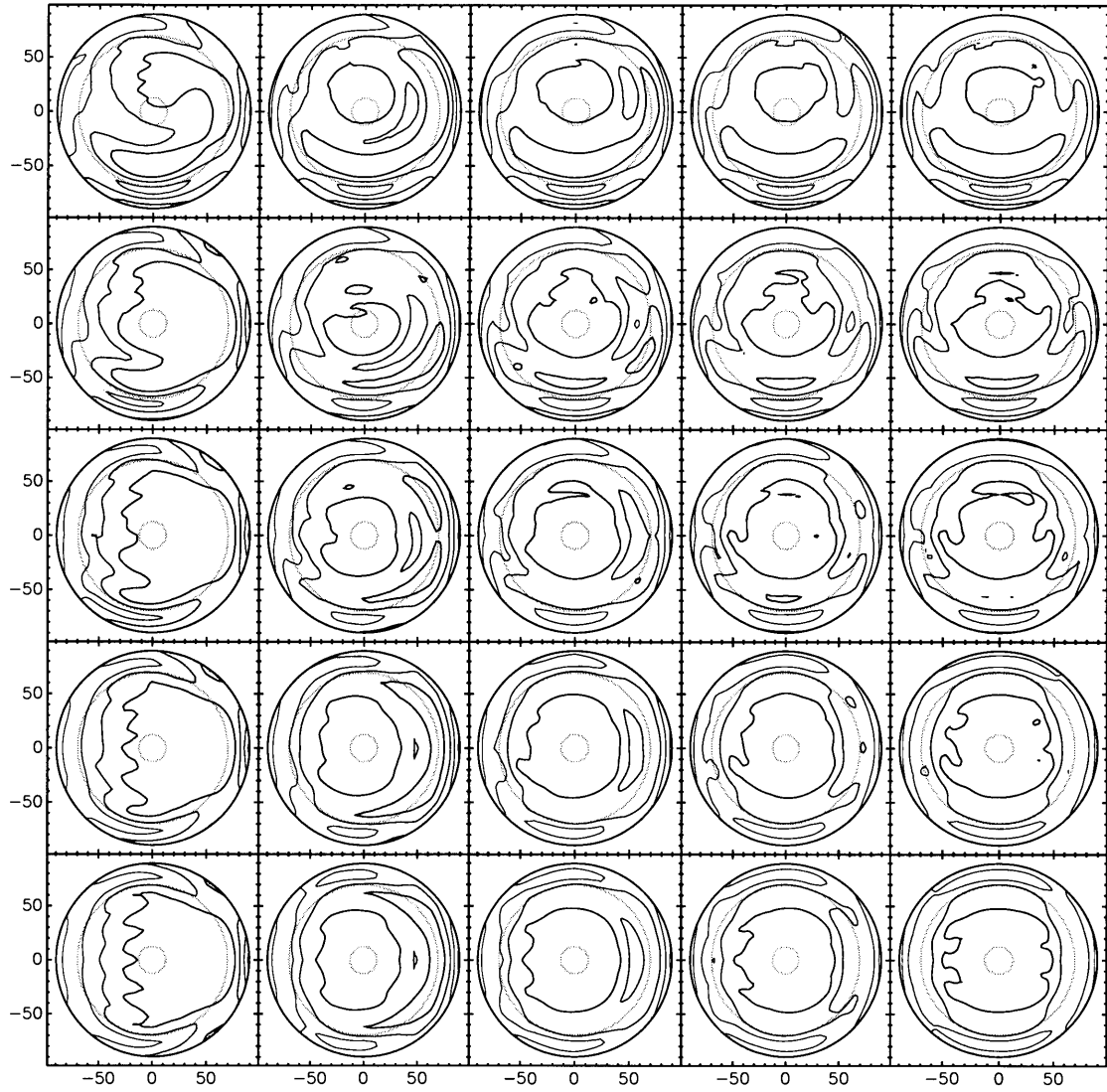


Figure 24: 25 element beam patterns at 760 MHz. Contours are drawn every 20% in voltage. The inner grey circles represent the angle subtended by the unpaneled portion of the primary. The outer grey circles represent the rim of the primary.

C Antenna patterns

Antenna patterns for the 25 unique elements identified in Figure 2 are shown for 311 MHz, 500 MHz, and 760 MHz in Figures 25, 26, and 27 respectively. Note their variation with frequency and position within the array.

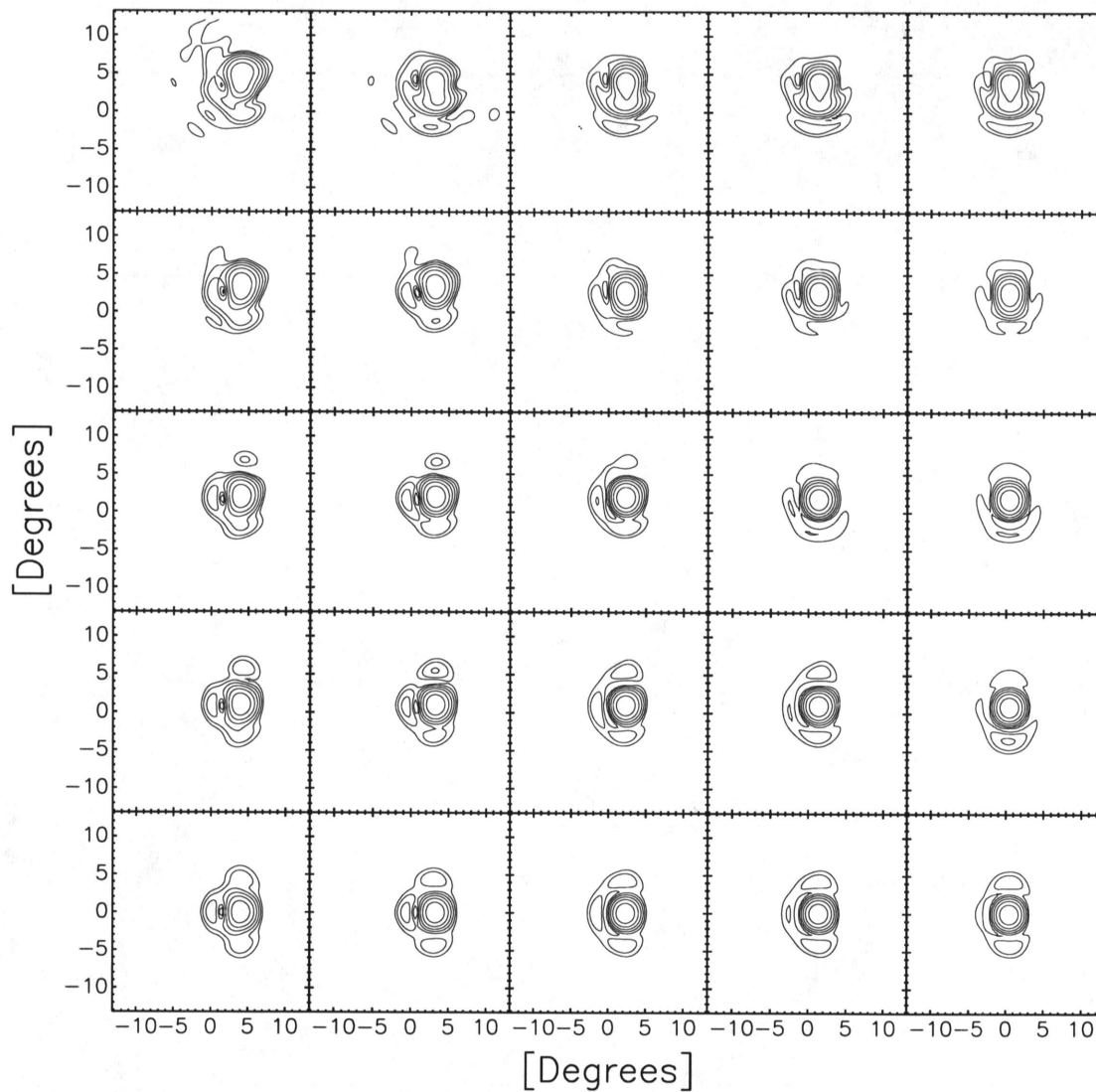


Figure 25: 25 antenna beam patterns corresponding to the 25 unique element patterns at 311 MHz. Contours are drawn at 3dB intervals

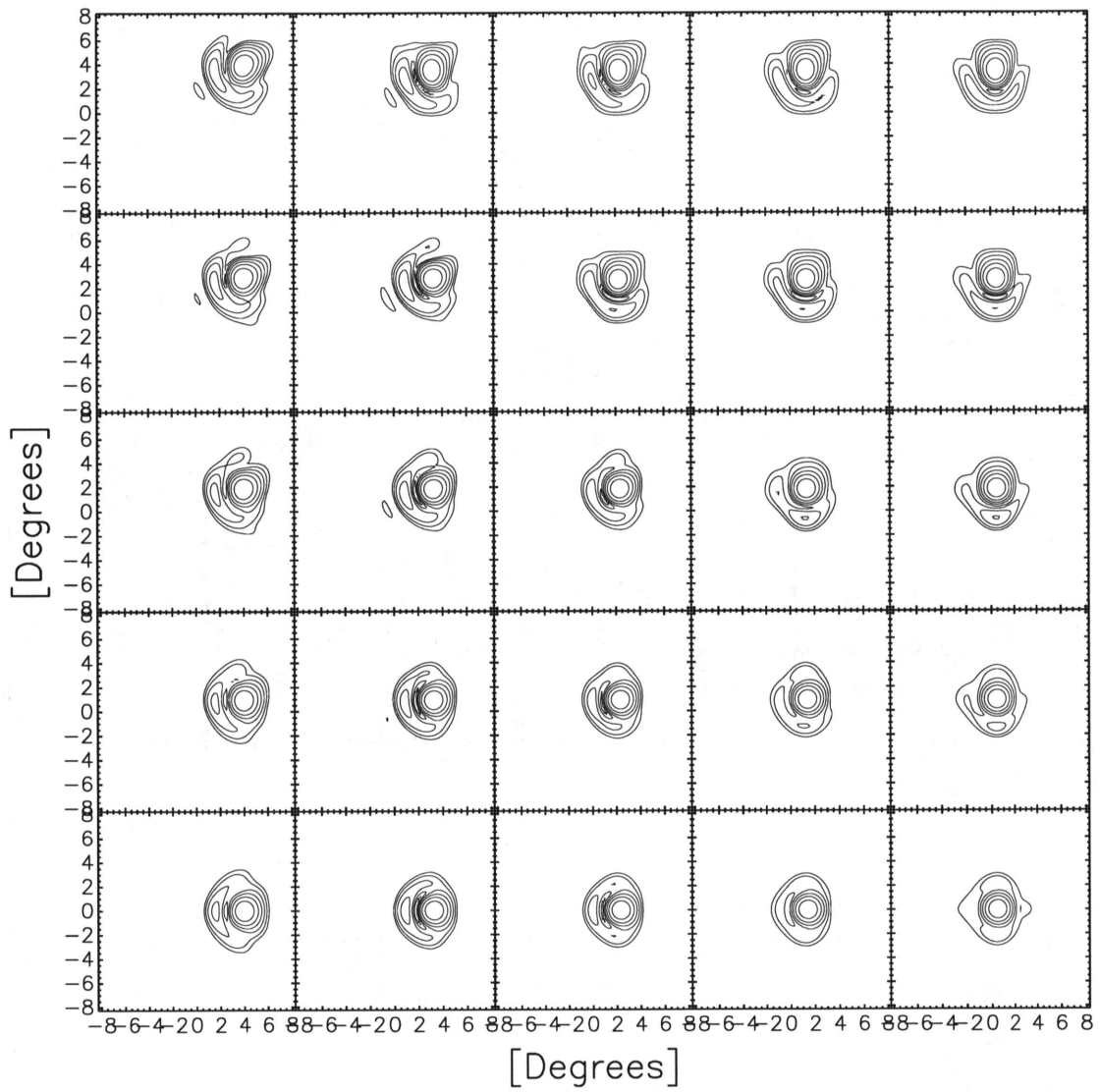


Figure 26: 25 antenna beam patterns corresponding to the 25 unique element patterns at 500 MHz.

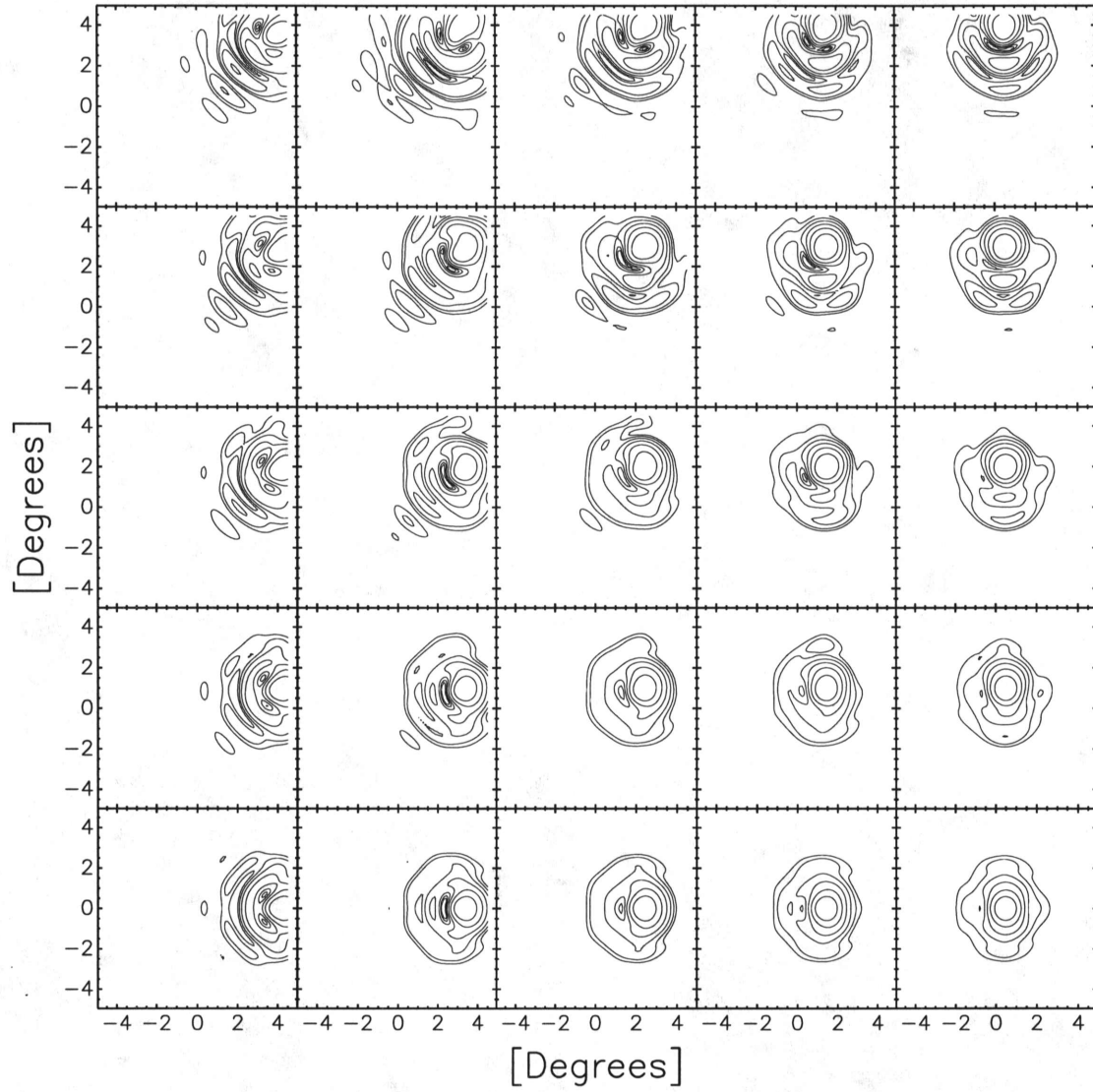


Figure 27: 25 antenna beam patterns corresponding to the 25 unique element patterns at 760 MHz.